IOP Publishing Smart Materials and Structures
Smart Mater. Struct. 24 (2015) 075016 (13pp) doi:10.1088/0964-1726/24/7/075016

A microplane constitutive model for shape memory alloys considering tension–compression asymmetry

M R Karamooz Ravari[1], M Kadkhodaei and A Ghaei

Department of Mechanical Engineering, Isfahan University of Technology, Isfahan, 84156-83111, Iran

E-mail: m.karamoozravari@me.iut.ac.ir, kadkhodaei@cc.iut.ac.ir and ghaei@cc.iut.ac.ir

Received 30 January 2015, revised 18 April 2015
Accepted for publication 27 April 2015
Published 4 June 2015

Abstract

Shape memory alloys are a group of advanced materials that have found several industrial applications due to their interesting mechanical properties including a shape memory effect and superelasticity. In order to optimize the use of such materials in manufacturing different devices, appropriate advanced constitutive models are required. Recent experiments show that shape memory alloys exhibit an asymmetric response during tension and compression loading. In this paper, a new three-dimensional constitutive law is proposed based on microplane theory with the purpose of describing the tension–compression asymmetry. The model utilizes an equivalent stress on the foundation of second and third invariants of the deviatoric stress tensor in combination with two internal variables to distinguish between martensite volume fraction as well as martensite elastic modulus during tension and compression. The proposed model is then used to simulate uniaxial tension–compression loading in superelasticity as well as ferroelasticity regimes. The simulation results are compared with the corresponding results obtained by experiment and previous models reported in the literature, and a good agreement is observed. In addition, a four-point bending test is simulated for NiTi tubes in several cases. The predicted moment–curvature response and variations in the position of the neutral axis correlate fairly well with the experimental findings reported in the literature.

Keywords: shape memory alloys, tension–compression asymmetry, microplane theory, superelasticity, shape memory effect, constitutive modeling

(Some figures may appear in colour only in the online journal)

1. Introduction

Nowadays, shape memory alloys (SMAs) are receiving a great deal of attention due to their exceptional mechanical and biological properties which make them good candidates for bone implants [1], energy absorbers [2], actuators [3, 4], and so on. The shape memory effect in these materials enables them to recover the applied deformations simply by heating them to above a specific temperature. In addition, if some amount of deformation is applied at high enough temperatures, the deformation will be totally recovered during unloading indicating superelasticity in these alloys. These phenomena happen because of the phase transformation from martensite to austenite and vice versa. In order to understand the thermomechanical behavior of SMA devices, appropriate constitutive models are required. Because these materials were first used in forms such as wires, beams, bars and rods, one-dimensional (1D) constitutive models were also developed by researchers [5–8]. By increasing the potential applications of SMAs such as load bearing implants, porous products and three-dimensional (3D) actuators, attempts for developing 3D constitutive models were also increased [9–14].

It is shown that SMAs exhibit an asymmetric mechanical behavior in tension and compression [15, 16]. To account for this intrinsic property, several 1D and 3D constitutive models

[1] Author to whom any correspondence should be addressed.

have been developed. In 3D constitutive models, some transformation functions were introduced based on the first invariant of the stress tensor, I_1, the second invariant of the deviatoric stress tensor, J_2, and the third invariant of the deviatoric stress tensor, J_3. Auricchio and Taylor [17] proposed a constitutive model to reproduce the superelastic behavior of SMAs at finite strains. To account for the pressure dependence of SMAs, they introduced a Drucker–Prager type loading function. Qidwai and Lagoudas [18] investigated various transformation functions to predict common characteristics of SMAs. To assess tension–compression asymmetry, they analyzed constitutive models in which J_2, J_2-I_1, J_2-J_3, and $J_2-J_3-I_1$ transformation functions were employed. Auricchio and Petrini [19] presented a 3D macroscopic thermomechanical model with the ability of reproducing tension–compression asymmetry using Prager–Lode type limit surface. Bouvet *et al* [20] proposed a phenomenological model by taking the tension–compression asymmetry into account using a transformation function based on J_2 and J_3 invariants. Paiva *et al* [21] proposed a constitutive model to consider superelasticity, one-way and two-way shape memory effect, phase transformation due to temperature variations, internal sub-loops due to incomplete phase transformations, and tensile–compressive asymmetry. Lagoudas *et al* [22] used averaging micromechanical methods based on the self-consistent approximation to model the thermomechanical behaviors of polycrystalline SMAs. They assessed several transformation functions to account for the tension–compression asymmetry as well as the development of a small volumetric strain during phase transformations. Lexcellent *et al* [23] proposed a modeling approach within the framework of thermodynamics of irreversible processes for the anisothermal response of shape memory alloys. A transformation function based on J_3 and J_2 invariants was used for considering the material asymmetry in tension and compression. Saint-Sulpice *et al* [24] investigated the superelastic behavior of SMAs under cyclic loadings. Material asymmetry was considered by utilizing the transformation function proposed in [20]. In order to scrutinize the effects of different loading modes on the superelastic behavior of SMAs, Zhu and Due [15] carried out some experiments on NiTi specimens under pure tension, compression, and torsion. They presented a macro-constitutive model for considering the tension–compression asymmetry of polycrystalline NiTi SMAs. Chao *et al* [25] constructed a micromechanical constitutive model to describe the cyclic deformation of polycrystalline NiTi SMAs in tensile and compressive loadings.

Mehrabi *et al* [26] used the microplane theory to develop a constitutive model for tension-torsion coupling and tension–compression asymmetry in NiTi shape memory alloys. In the case of material asymmetry, they employed a modified phase diagram for uniaxial loading and chose the material parameters based on the loading direction, i.e. tension or compression. Since there is no transformation function, this method can be used only for uniaxial loading and would be inapplicable for multiaxial loadings. The idea of utilizing microplane theory was first proposed by Brocca *et al* [27] and has been further developed by Kadkhodaei *et al* [28, 29] and Mehrabi *et al* [30]. This constitutive modeling approach was shown to be thermodynamically consistent [31] and capable of modeling nonproportional loading paths [28–30, 32]. One of the most important features of microplane theory is its capability to generalize a 1D constitutive model to a 3D one. Therefore, one just needs the material parameters identified through a uniaxial tension (or compression) test for modeling 3D loading cycles. According to the existing findings, this modeling approach provides a simple yet powerful 3D constitutive modeling approach for SMAs. However, it is necessary to enhance it to be able to systematically consider the tension–compression asymmetric response of SMAs. In addition, it has been previously shown that the elastic modulus of the martensite phase is different in tension and compression [33]. However, the available 3D constitutive models have not addressed this behavior. The aim of this paper is to address these issues. To this end, two internal state variables are considered to distinguish between martensite volume fraction in tension and compression using a modified phase diagram and evolution functions. The obtained results in uniaxial tension–compression and four-point bending of NiTi tubes are compared with experimental results and good correlations were observed. Therefore, the proposed model can be used as an appropriate tool for modeling 3D responses of shape memory alloys considering tension–compression asymmetry.

2. Constitutive modeling

In microplane modeling, a 1D constitutive law is used for any generic plane, referred to as a microplane, passing through any material point. To generalize the 1D constitutive model to the 3D one, a homogenization process is used. Therefore, only the material parameters of the uniaxial tension (or compression) test are required for the 3D model, which makes this method of more interest. In this section, first, a 1D constitutive relation of SMAs considering tension–compression asymmetry is introduced. Then, this 1D law is generalized to a 3D model by using microplane theory and a suitable transformation function.

2.1. One-dimensional constitutive model

According to the approach proposed by Poorasadion *et al* [33], considering the tension–compression asymmetry, the 1D stress–strain relation of a SMA can be described using the following equation:

$$\sigma = E\left(\varepsilon - \varepsilon_L^+\xi_s^+ - \varepsilon_L^-\xi_s^-\right) \tag{1}$$

in which ξ_s and ε_L are the stress-induced martensite volume fraction and maximum recoverable strain, respectively. The superscripts '+' and '–' denote tension and compression, respectively. σ and ε are respectively the uniaxial stress and strain, and E the elastic modulus. It is shown that the elastic modulus of SMAs is a function of the martensite volume

fraction and can be written using the Reuss model as follows:

$$\frac{1}{E} = \frac{1}{E_{\mathrm{A}}} + \xi_s^{+}\left(\frac{1}{E_{\mathrm{M}}^{+}} - \frac{1}{E_{\mathrm{A}}}\right) + \xi_s^{-}\left(\frac{1}{E_{\mathrm{M}}^{-}} - \frac{1}{E_{\mathrm{A}}}\right) + \xi_{\mathrm{T}}\left(\frac{1}{E_{\mathrm{M}}^{T}} - \frac{1}{E_{\mathrm{A}}}\right) \tag{2}$$

where E_{A} and E_{M} are the elastic moduli of full austenite and full martensite phases, respectively, and ξ_{T} the temperature-induced martensite volume fraction. The superscript 'T' is attributed to temperature-induced quantities.

To specify the evolution of $\xi_s^{\pm}$, and ξ_{T}, the evolution function presented by eqution (3) is utilized. This evolution function was firstly proposed by Brinson [6] and then modified by Poorasadion *et al* [33] to account for the tension–compression asymmetry. In this paper, this evolution function is enhanced to model the start and finish of the reverse transformation more accurately with the use of the stress-temperature phase diagram depicted in figure 1 [34].

$$\begin{cases}
\text{if } T \leqslant M_{\mathrm{s}} \text{ and } \sigma_{\mathrm{s}}^{\mathrm{cr}} < \hat{\sigma} < \sigma_{\mathrm{f}}^{\mathrm{cr}} \\
Y = \cos\left(\dfrac{\pi}{\sigma_{\mathrm{f}}^{\mathrm{cr}} - \sigma_{\mathrm{s}}^{\mathrm{cr}}}\left(\hat{\sigma} - \sigma_{\mathrm{s}}^{\mathrm{cr}} - C_{\mathrm{M}}(T - M_{\mathrm{s}})\right)\right) \\
\xi_s^r = \dfrac{1-y}{2} + \xi_{s0}^r\dfrac{1+y}{2},\ \xi_s^p = \xi_{s0}^p\dfrac{1-\xi_s^r}{1-\xi_{s0}^r}, \\
\xi_{\mathrm{T}} = \left(\xi_{\mathrm{T0}} + \Delta\right)\dfrac{\left(1-\xi_s^r\right)}{1-\xi_{s0}^r} \\
\text{if } T < M_{\mathrm{f}}\text{: } \Delta = 0 \\
\text{else: } \Delta = \dfrac{1-\xi_0}{2}\left(1 - Y_{\mathrm{MT}}\right) \\
\text{if } T > M_{\mathrm{s}} \text{ and } \sigma_{\mathrm{s}}^{\mathrm{cr}} + C_{\mathrm{M}}\left(T - M_{\mathrm{s}}\right) < \hat{\sigma} < \sigma_{\mathrm{f}}^{\mathrm{cr}} \\
\qquad + C_{\mathrm{M}}\left(T - M_{\mathrm{s}}\right)\text{:} \\
Y = \cos\left(\dfrac{\pi}{\sigma_{\mathrm{f}}^{\mathrm{cr}} - \sigma_{\mathrm{s}}^{\mathrm{cr}}}\left(\hat{\sigma} - \sigma_{\mathrm{s}}^{\mathrm{cr}} - C_{\mathrm{M}}\right)\left(T - M_{\mathrm{s}}\right)\right) \\
\xi_s^r = \dfrac{1-Y}{2} + \xi_{s0}^r\dfrac{1+Y}{2},\ \xi_s^p = \xi_{s0}^p\dfrac{1-\xi_s^r}{1-\xi_{s0}^r}, \\
\xi_{\mathrm{T}} = \xi_{\mathrm{T0}}\dfrac{1-\xi_s^r}{1-\xi_{s0}^r} \\
\text{if } T > A_{\mathrm{s}} \text{ and } C_{\mathrm{Af}}\left(T - A_{\mathrm{f}}\right) < \hat{\sigma} < C_{\mathrm{As}}\left(T - A_{\mathrm{s}}\right)\text{:} \\
Y = \cos\left(\dfrac{\pi}{C_{\mathrm{As}}\left(T - A_{\mathrm{s}}\right) - C_{\mathrm{Af}}\left(T - A_{\mathrm{f}}\right)} \times \left(C_{\mathrm{As}}\left(T - A_{\mathrm{s}}\right) - \hat{\sigma}\right)\right) \\
\xi_s^r = \dfrac{\xi_{s0}^r}{2}\left(1 + Y\right),\ \xi_s^p = \dfrac{\xi_{s0}^p}{2}\left(1 + Y\right), \\
\xi_{\mathrm{T}} = \dfrac{\xi_{\mathrm{T0}}}{2}\left(1 + Y\right) \\
\text{if } M_{\mathrm{f}} < T < M_{\mathrm{s}} \text{ and } \hat{\sigma} < \sigma_{\mathrm{s}}^{\mathrm{cr}} \\
\xi_s^r = \xi_{s0}^r,\quad \xi_s^p = \xi_{s0}^p,\ \xi_{\mathrm{T}} = \dfrac{1-\xi_0}{2}\left(1 - Y_{\mathrm{MT}}\right) + \xi_{\mathrm{T0}}
\end{cases} \tag{3}$$

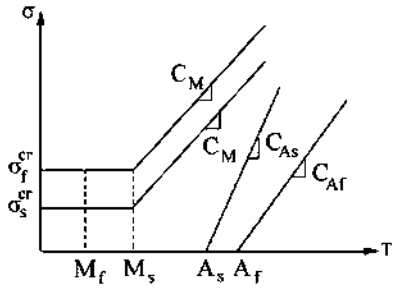

Figure 1. The stress-temperature diagram for the martensite transformation of shape memory alloys.

in which M_{f}, M_{s}, A_{s}, A_{f}, and T are martensite finish, martensite start, austenite start, austenite finish, and temperature, respectively. Superscripts 'r' and 'p' are as ($r=+$, $p=-$) in tension and ($r=-$, $p=+$) in compression, $\sigma_{\mathrm{s}}^{\mathrm{cr}}$and $\sigma_{\mathrm{f}}^{\mathrm{cr}}$ the critical start and finish stresses for martensite detwinning, ξ_{s0}^r, ξ_{s0}^p, and ξ_{T0} the initial values of the corresponding martensite volume fraction, C_{M}, C_{As}, and C_{Af} the slopes of the transformation strips as shown in figure 1, and $Y_{\mathrm{MT}} = \cos\left(\pi\left(T - M_{\mathrm{s}}\right)/\left(M_{\mathrm{f}} - M_{\mathrm{s}}\right)\right)$. $\hat{\sigma}$ is the modified stress to account for the asymmetry in tension and compression as follows:

$$\hat{\sigma} = \frac{1 \pm \beta}{1 + \beta}\sigma \tag{4}$$

where '+' and '–' in the numerator indicate tension and compression, respectively, and β is a parameter to determine the value of asymmetry, which is defined using the following relation:

$$\beta = \begin{cases} \beta_1 \text{ if } \dot{\sigma} > 0 \\ \beta_2 \text{ if } \dot{\sigma} < 0 \end{cases} \tag{5}$$

in which β_1 and β_2 are chosen to distinguish the asymmetry level of loading from that of unloading. The effect of β on the asymmetry level will be discussed in the following section.

When using the phase diagram at high temperatures, if the values of C_{As} and C_{Af} are higher than C_{M}, it should be noted that the corresponding lines may cross each other. This issue would be problematic when the critical stress of austenite finish is higher than that of martensite start or if the critical stress of austenite start is higher than that of martensite finish. Figures 2(a) and (b) demonstrate these cases, respectively. It implies some restrictions on the transformation stresses as presented by equations (6) and (7):

$$C_{\mathrm{As}}\left(T - A_{\mathrm{s}}\right) < \sigma_{\mathrm{cr}}^{\mathrm{f}} + C_{\mathrm{M}}\left(T - M_{\mathrm{s}}\right) \tag{6}$$

$$C_{\mathrm{Af}(T-A_{\mathrm{f}})} < \sigma_{\mathrm{cr}}^{\mathrm{s}} + C_{\mathrm{M}}\left(T - M_{\mathrm{s}}\right) \tag{7}$$

According to the above-mentioned explanations and considering $\boldsymbol{M_{\mathrm{d}}}$ as the martensite dead temperature, the phase diagram should be used for temperatures with the constraint

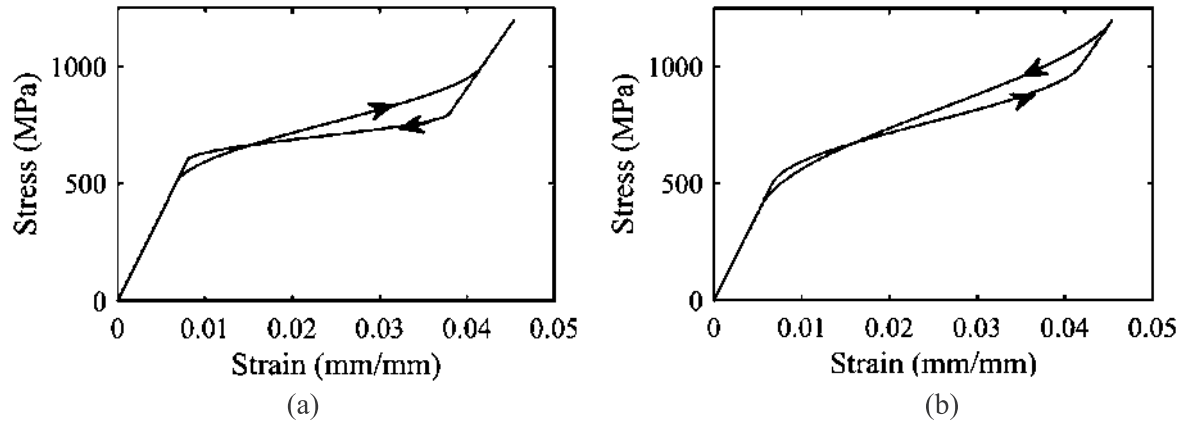

Figure 2. The stress–strain curve of an SMA when (a) the critical stress of austenite finish is higher than that of start martensite, and (b) the critical stress of austenite start is higher than that of martensite finish.

below:

$$T < \min\left(\frac{\left(C_{\mathrm{Af}}A_{\mathrm{f}} + \sigma_{\mathrm{cr}}^{\mathrm{s}} - C_{\mathrm{M}}M_{\mathrm{s}}\right)}{C_{\mathrm{Af}} - C_{\mathrm{M}}}, \frac{\left(C_{\mathrm{As}}A_{\mathrm{s}} + \sigma_{\mathrm{cr}}^{\mathrm{f}} - C_{\mathrm{M}}M_{\mathrm{s}}\right)}{C_{\mathrm{As}} - C_{\mathrm{M}}}, M_{\mathrm{d}}\right) \tag{8}$$

2.2. Three-dimensional constitutive model

To develop a 3D constitutive model using the microplane theory, three main steps should be followed. These steps are the projection of the macroscopic stress tensor on each microplane, the definition of a 1D constitutive law for each microplane, and the generalization of 1D constitutive laws to 3D using a homogenization process [28–31]. In this regard, a static constraint formulation with a volumetric-deviatoric split is employed in the present work. As shown in figure 3, the macroscopic stress tensor may be projected as normal and shear vectors on a microplane. The normal and shear stresses on each microplane can be described as:

$$\sigma_{\mathrm{N}} = N_{ij}\sigma_{ij} \tag{9}$$

$$\sigma_{\mathrm{T}} = T_{ij}\sigma_{ij} \tag{10}$$

where σ_{ij} is the macroscopic stress tensor, σ_{N} normal stress, σ_{T} shear stress, $N_{ij} = n_i n_j$, $T_{ij} = \left(t_i n_j + t_j n_i\right)/2$ in which $t_i = (\sigma_{ik}n_k - \sigma_{\mathrm{N}}n_i)/\sqrt{\sigma_{jr}\sigma_{js}n_r n_s - \sigma_{\mathrm{N}}^2}$ is the unit vector parallel to the resultant shear stress on the plane, and $\mathrm{n_i}$ are the components of the unit normal vector, $\boldsymbol{n}$, to a microplane. The normal stress is split into volumetric and deviatoric parts as:

$$\sigma_{\mathrm{N}} = \sigma_{\mathrm{V}} + \sigma_{\mathrm{D}} \tag{11}$$

in which $\sigma_{\mathrm{V}} = \delta_{ij}\sigma_{ij}/3$, $\sigma_{\mathrm{D}} = \left(N_{ij} - \delta_{ij}/3\right)\sigma_{ij}$, and δ_{ij} is the *Kronecker delta*. It is shown that using the volumetric-deviatoric split, the micro-level elastic moduli are equal to the macroscopic ones [27, 28]. It is also supposed that the martensite transformation is just associated with the shear component of microplane stresses [28, 29]. Accordingly, the volumetric and deviatoric parts are described using Hooke's law, and the shear stress can be described using eqution (1) as follows:

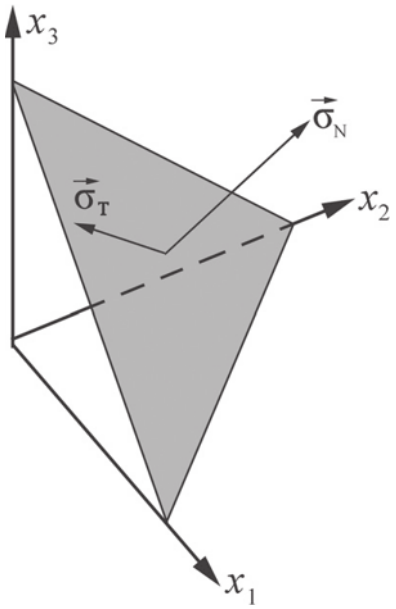

Figure 3. Projection of stress tensor as normal and shear stress vectors on each micro plane.

$$\varepsilon_{\mathrm{V}} = \frac{1-2\nu}{E}\sigma_V \tag{12}$$

$$\varepsilon_{\mathrm{D}} = \frac{1+\nu}{E}\sigma_D \tag{13}$$

$$\varepsilon_{\mathrm{T}} = \frac{1+\nu}{E}\sigma_T + \varepsilon_L^+\xi_s^+ + \varepsilon_L^-\xi_s^- \tag{14}$$

where ν is the SMAs Poisson ratio, ε_{V} the volumetric strain, ε_{D} the deviatoric strain, and ε_{T} the shear strain. By applying the principle of complementary virtual work [28, 29] and some simplifications, the following relation is obtained for the

strain tensor:

$$\varepsilon_{ij} = -\frac{\nu}{E}\sigma_{mm}\delta_{ij} + \frac{1+\nu}{E}\sigma_{mn}\cdot\frac{3}{2\pi}\int_{\Omega}\left(N_{mn}N_{ij} + T_{mn}T_{ij}\right)\mathrm{d}\Omega + \left(\varepsilon_L^{+}\xi_s^{+} + \varepsilon_L^{-}\xi_s^{-}\right)\cdot\frac{3}{2\pi}\int_{\Omega}T_{ij}\mathrm{d}\Omega. \quad (15)$$

To consider the material asymmetry in tension and compression, it is necessary to define an appropriate equivalent stress to be used in equation (3) for evaluating the martensite volume fractions in equation (14). In this paper, an equivalent stress based on second and third invariants of deviatoric stress tensor (J_2 and J_3) is used as demonstreated below [15, 19, 22]:

$$\hat{\sigma} = \frac{1}{1+\beta}\left\{\sqrt{3J_2} + \frac{9}{2}\beta\frac{J_3}{J_2}\right\} \quad (16)$$

in which J_2 and J_3 are the second and third invariants of the deviatoric stress tensor, respectively. Note that, equation (16) reduces to equation (4) for 1D cases. Figure 4 shows the transformation surfaces for different typical values of β in the plane stress state. As it is obvious, when $\beta = 0$, the symmetric transformation surface is achieved. By increasing the value of β, the level of asymmetry will increase. According to experimental observations, the transformation surface of martensite-to-austenite and austenite-to-martensite might be of a different level of asymmetry. This can be taken into account by using different values of β presented in equation (5).

3. Results and discussion

The proposed 3D constitutive model is implented through a user subroutine UMAT in the ABAQUS comertial finite element package. To verify the model, six available experimental cases in the literature including two uniaxial tension–compression tests, two ferroelasticity problems, and two four-point bending tests of NiTi tubes are considered. One case related to subloops due to incomplete phase transformations is also investigated and the results are compared with experimenal findings. Notice that, since all the simulations are carried out at constant temperatures, there is not any temperature-induced martensite during the loading cycles. Accordingly, the value of E_{M}^{T} is optional in the nuemrical simulations.

3.1. Uniaxial tests

In this subsection, the experimental tension–compression responses of superelastic NiTi samples provided by Zhu and Dui [15] (case 1) and Thamburaja and Anand [35] (case 2) are used for verification of the model. For these cases, the material is 50.8at.% NiTi and 55.96 wt.% NiTi, respectively. Tables 1 and 2 show the material parameters utilized for the determination of the stress–strain response in cases 1 and 2, respectively. These material parameters are obtained from the literature [15, 36]. Since the test temperature is above the austenite finish, the material is in the austenite phase; so, the initial value for ξ_{s0}^{+}, ξ_{s0}^{-}, and ξ_{T0} is zero for these two cases.

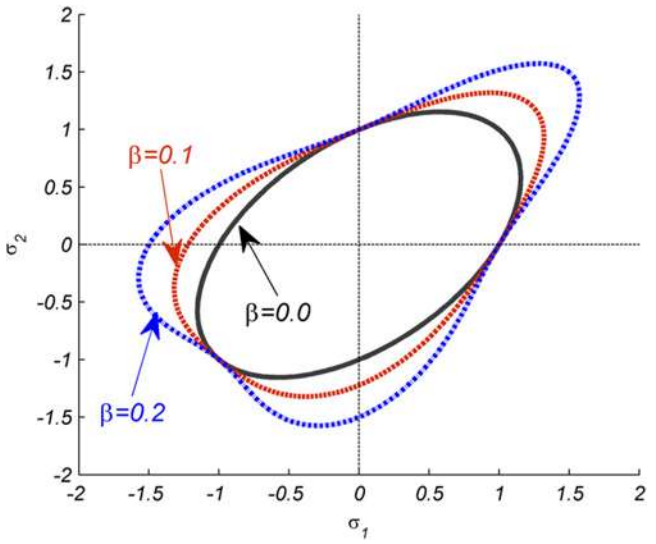

Figure 4. Transformation surface in plane–stress state for different typical values of β.

Figures 5 and 6 show the stress–strain response of NiTi samples in tension and compression obtained using the proposed approach, the Zhu and Dui model, and the experimental measurements [15, 35]. In all cases, the absolute values of the stress and strain are reported in compression tests. The results show a good agreement between the empirical findings and the numerical results of the present approach. In comparison with the Zhu and Dui model, the proposed model correlates better to the experimental findings especially during unloading. It is because of using the modified phase diagram (figure 1) which allows one to adjust the start and finish martensite–austenite transformation stresses more adaptively. As demonstrated in figure 5, since the elastic modulus of martensite is considered to be different in tension and compression, the proposed model is able to reproduce the experimental stress–strain response in compression more accurately. However, there is a considerable mismatch between the numerical and experimental tensile stress–strain responses at the first portion of the loading curve in figure 5. This is due to different experimental values of the austenite elastic modulus in tension and compression. In figure 5, the value of the austenite elastic modulus is calibrated using the compressive stress–strain response to be able to compare the results with those reported in [15]. Zhu and Dui [15] suggest the use of a compressive stress–strain curve to calibrate the model parameters because the transformation is more stable during unloading in the case of compression compared with tension. In addition, in all the experimental cases, there is a small amount of residual strain due to the transformation induced plasticity (TRIP) phenomenon, which can be reduced by training the SMA specimen through cyclic loading. Since the present model is not capable of considering the effect of TRIP, there is not any residual strain in the predicted stress–strain response.

Table 1. Material parameters for case 1 [15].

E_A (MPa)	E_M^+ (MPa)	E_M^- (MPa)	ν	M_f (K)	M_s (K)	A_s (K)	A_f (K)	σ_s^{cr} (MPa)
24 000	22 000	25 000	0.42	200.3	232.3	262.5	295.1	0
σ_f^{cr} (MPa)	C_M (MPa/K)	C_{As} (MPa/K)	C_{Af} (MPa/K)	ε_L^+	ε_L^-	β_1	β_2	T (K)
180	3.37	3.7	2	0.052	–0.023	0.165	0.165	299.1

Table 2. Material parameters for case 2 [36].

E_A (MPa)	E_M^+ (MPa)	E_M^- (MPa)	ν	M_f (K)	M_s (K)	A_s (K)	A_f (K)	σ_s^{cr} (MPa)
71 000	35 000	42 000	0.33	213	251.3	260.3	268.5	256
σ_f^{cr} (MPa)	C_M (MPa/K)	C_{As} (MPa/K)	C_{Af} (MPa/K)	ε_L^+	ε_L^-	β_1	β_2	T (K)
288	4.28	5.73	4.07	0.048	-0.031	0.13	0.13	298

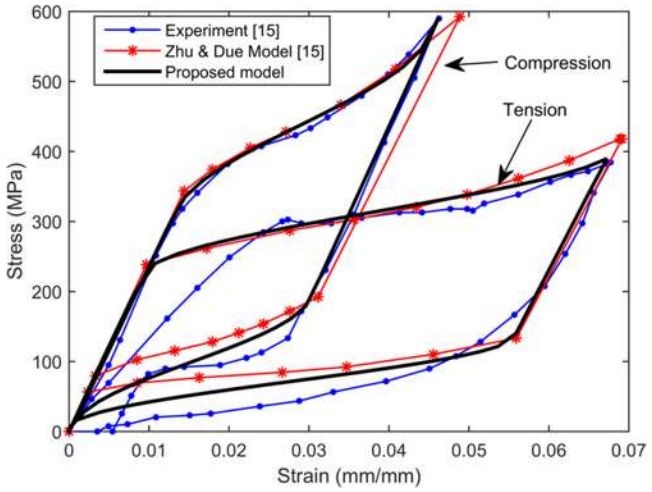

Figure 5. The experimental and numerical stress–strain responses for case 1.

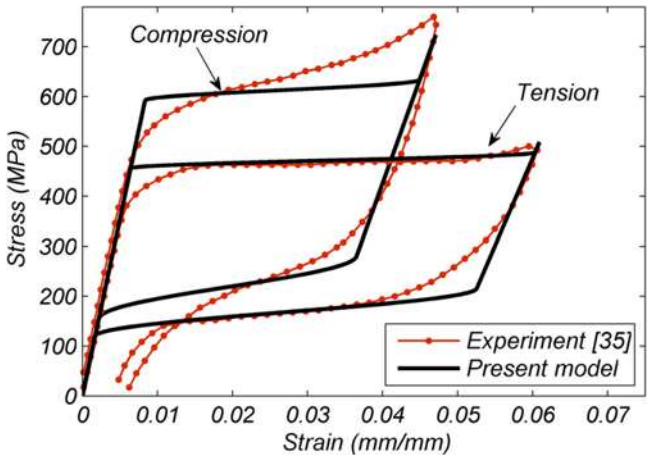

Figure 6. The experimental and numerical stress–strain response for case 2.

In order to show the capability of the model to consider the effects of tension–compression asymmetry in ferroelastic behavior, the stress–strain responses obtained using the proposed model are compared with the numerical results reported by Jaber *et al* [36] (case 3) and the experimental findings for Au-47.5at.%Cd by Nakanishi *et al* [37] (case 4). The material parameters used for the former and the latter cases are provided in tables 3 and 4, respectively. In case 3, the temperature is below A_s and the material is initially fully austenitic, which means the initial values of $\xi_{s0}^+ = \xi_{s0}^- = \xi_{T0} = 0$. For case 4, the temperature is below the martensite finish temperature and the material is initially in the martensite phase which causes $\xi_{s0}^+ = \xi_{s0}^- = 0$ and $\xi_{T0} = 1$. The result of the present model are compared with the previously reported findings by Jaber *et al* [36] and the experimental data by Nakanishi *et al* [37] in figures 7(a) and (b), respectively. The obtained stress–strain responses show that the present approach is in good agreement with the previously proposed model and experiments. Since the proposed model by Jaber *et al* [36] is not capable of considering different values for martensite elastic moduli in tension and compression as well as different values for C_A, it is assumed that $E_M^+ = E_M^-$ and $C_{As} = C_{Af}$ to be able to compare the results.

The stress–strain response presented in figure 7(b) shows that the model is capable of modeling subloops due to incomplete phase transformations for test temperature below martensite finish temperature. To show the ability of the model in reproducing this behavior for temperatures above austenite finish, the experimental results for 50.95at.%NiTi reported by Takeda *et al* [38] (case 5) are used. Figure 8 shows a comparison of the stress–strain response reproduced by the proposed model and the experimental results [38]. The material parameters utilized for this simulation are presented in table 5 and the initial conditions are as $\xi_{s0}^+ = \xi_{s0}^- = \xi_{T0} = 0$. Since the test is just performed in tension, the material parameters related to compression are not provided. Referring to figures 7(b) and 8, the present model can be used for modeling the internal subloops of an SMA in a wide range of temperatures.

3.2. Four-point bending of tubes

In this subsection, the proposed model is used to simulate four-point bending of NiTi tubes. First, the finite element modeling of the four-point bending is described. Then, the procedure of finding material parameters for two different cases, named cases 6 and 7, is explained. Finally, the results

Table 3. Material parameters for case 3 [36].

E_A (MPa)	E_M^+ (MPa)	E_M^- (MPa)	ν	M_f (K)	M_s (K)	A_s (K)	A_f (K)	σ_s^{cr} (MPa)
80 000	30 000	30 000	0.33	273	283	293	303	105
σ_f^{cr} (MPa)	C_M (MPa/K)	C_{As} (MPa/K)	C_{Af} (MPa/K)	ε_L^+	ε_L^-	β_1	β_2	T (K)
225	5	5	5	0.0615	–0.046	0.186	0.186	285

Table 4. Material parameters for case 4 [37].

E_A (MPa)	E_M^+ (MPa)	E_M^- (MPa)	ν	M_f (K)	M_s (K)	A_s (K)	A_f (K)	σ_s^{cr} (MPa)
5000	5000	5000	0.33	308	331	345	358	11
σ_f^{cr} (MPa)	C_M (MPa/K)	C_{As} (MPa/K)	C_{Af} (MPa/K)	ε_L^+	ε_L^-	β_1	β_2	T (K)
44	2	2	2	0.032	–0.034	–0.16	–0.16	300

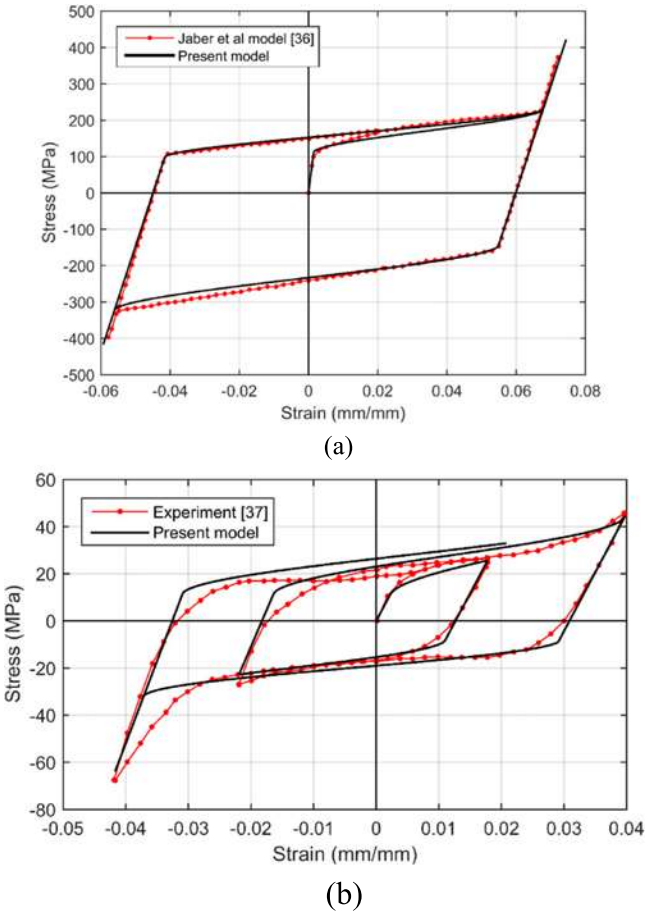

Figure 7. Comparison of the obtained ferroelastic stress–strain response with (a) numerical results reported by Jaber *et al* [36] and (b) experimental results by Nakanishi *et al* [37].

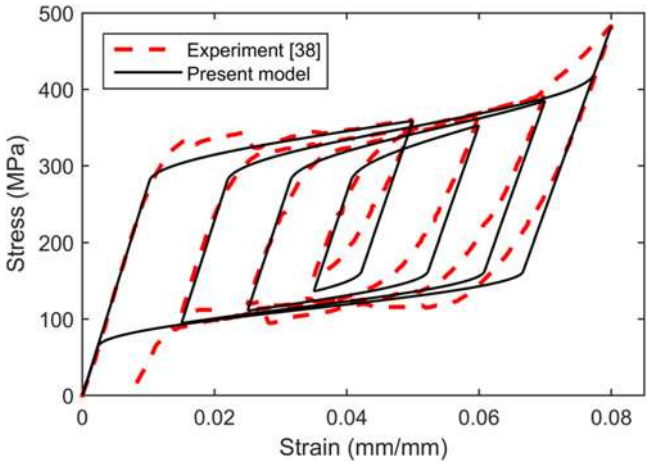

Figure 8. Stress–strain response related to subloops due to incomplete phase transformation.

of the numerical simulations are presented and discussed for both cases.

Consider a tube with length L, gage length L_e, outer diameter D, and thickness t as shown in figure 9(a) which depicts the schematic of the four-point bending test. The four loading points are circular rollers which hold the tube in the bending plane. Each pair of rollers is fixed to a loading wheel. These loading wheels are loaded by two cables and rotate around their center which cause bending of the tube. The magnitude of the applied moment can be calculated by measuring the force in the cable, F. A gage with length L_e is attached at the middle of the tube to measure the rotation angle due to the applied moment. More information about the test apparatus and method are provided [39, 40]. As shown in figure 9(b), the mean curvature of the tube, κ, can be calculated by measuring the angles of rotation at the tube's ends (θ) and using the following equation:

$$\kappa = \frac{\theta}{L_e} \tag{17}$$

Because the problem is symmetric about the $z=0$ plane, only half of the tube is modeled and appropriate boundary conditions are imposed. Referring to figure 10, a tube with length $L_e/2$ is considered for modeling purposes because the response of the tube in the gage region is of concern. Due to the symmetry about the $z=0$ plane, this plane should not move toward the z direction and the slope of the tube would be zero at this point. Accordingly, at one end (symmetry plane) of the half tube, the translational degree of freedom in the z direction and all rotational degrees of freedom are fixed. Referring to figure 9(a), the tube at the end of the gage length rotates with the angle of θ due to the applied moment. To

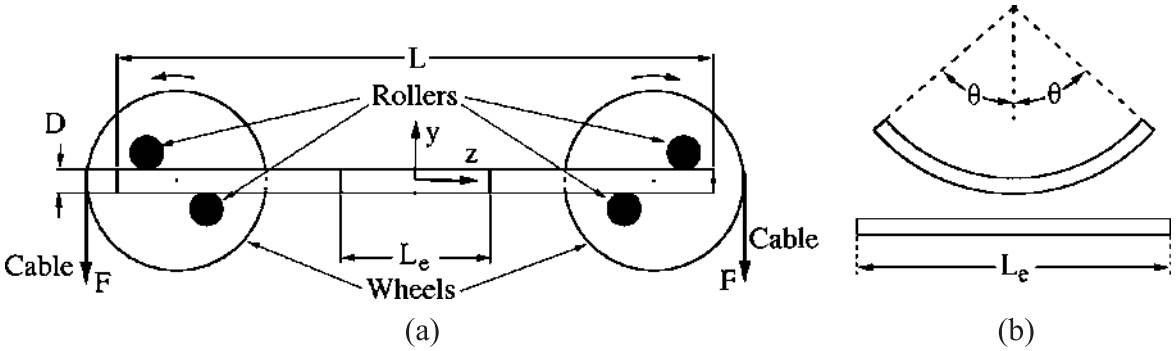

Figure 9. (a) Schematic configuration of the four-point bending test and (b) illustration of the curvature calculation method.

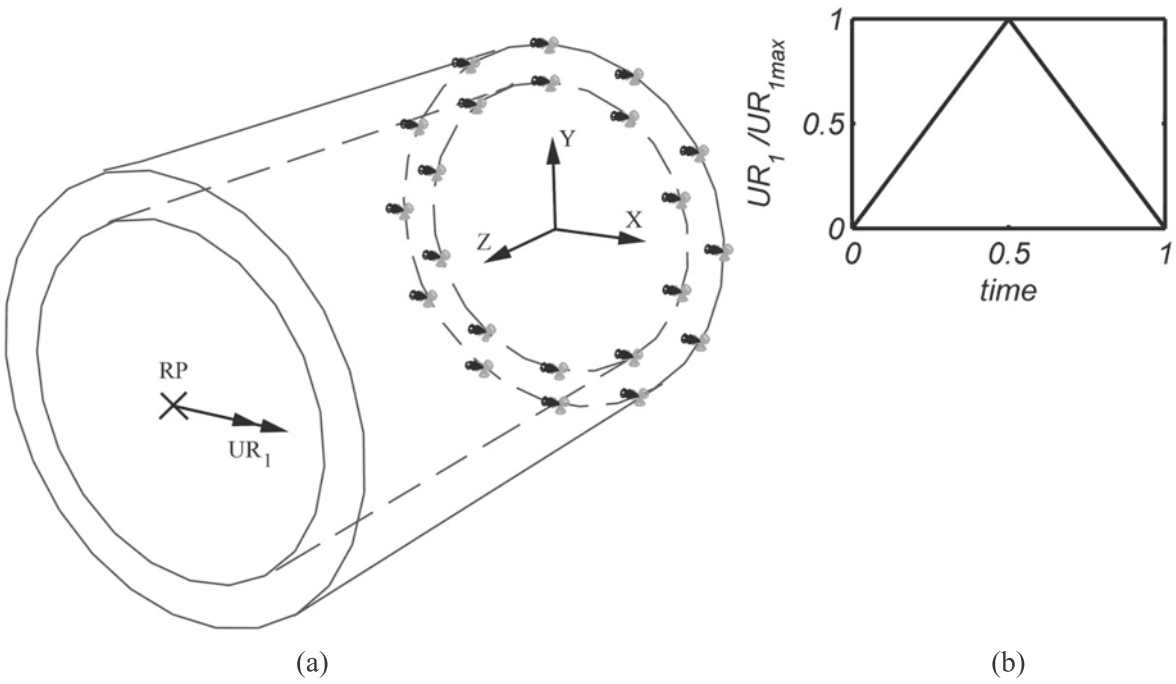

Figure 10. (a) Boundary conditions and loading in the four-point bending model and (b) the amplitude variation of the reference point rotation.

Table 5. Material parameters for case 5.

E_A (MPa)	E_M^+ (MPa)	E_M^- (MPa)	ν	M_f (K)	M_s (K)	A_s (K)	A_f (K)	σ_s^{cr} (MPa)
27 600	24 000	NA	0.3	100	220	254	281	100
σ_f^{cr} (MPa)	C_M (MPa/K)	C_{As} (MPa/K)	C_{Af} (MPa/K)	ε_L^+	ε_L^-	β_1	β_2	T (K)
240	2.31	3.7	3.8	0.062	NA	NA	NA	298

model this rotation, at this end, a reference point is defined and all nodes of that end are tied to the reference point. A rotation about the x-axis, UR_1, is applied to the reference point using the amplitude variation shown in figure 10(b). In addition, the history of the reaction moment in response to the applied amount of rotation is requested to be able to depict the moment-rotation diagrams.

In this paper, the experimental results reported by Reedlunn *et al* [40] and Bechle and Kyriakides [39] are used for comparison. These experimental measurements are performed isothermally using a cold-drawn, slightly Ni-rich NiTi tube from the Memry Corporation [39, 40]. For the sake of simplicity, in the rest of the paper, the former and the latter

Table 6. Geometric information of cases 6 and 7.

Dimension	L_e (mm)	D (mm)	t (mm)
Case 4	9.58	3.176	0.318
Case 5	76.7	5.11	0.625

Table 7. Material parameters obtained by calibration of stress–strain response in tension and compression for case 6.

E_A (MPa)	E_M^+ (MPa)	E_M^- (MPa)	ν	M_f (K)	M_s (K)	A_s (K)	A_f (K)	σ_s^{cr} (MPa)
65 300	28 000	87 000	0.45	126	210	248	292	90
σ_f^{cr} (MPa)	C_M (MPa/K)	C_{As} (MPa/K)	C_{Af} (MPa/K)	ε_L^+	ε_L^-	β_1	β_2	T (K)
170	3.65	4.5	32	0.054	–0.035	0.23	0.23	298

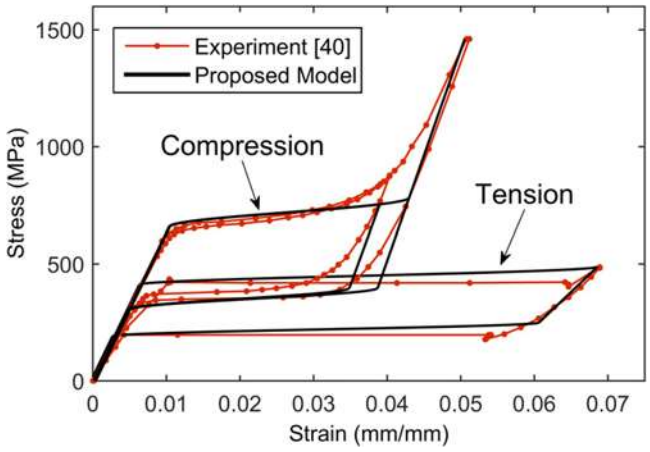

Figure 11. The experimental and numerical stress–strain curve of NiTi tube in tension and compression for case 6.

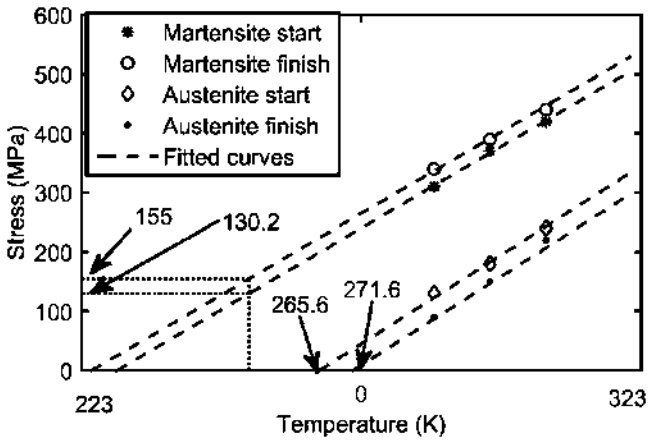

Figure 12. The obtained phase diagram for the tube used in experiments by Bechle and Kyriakides [39].

cases are denoted by case 6 and case 7, respectively. Table 6 shows the geometric details of these two cases.

Similar to cases 1 and 2, the test temperature is higher than the austenite finish temperature and the initial phase is austenite for cases 6 and 7. Therefore, the same initial conditions are used for these simulations. To attribute suitable material parameters to the finite element model, the experimental stress–strain response in uniaxial tension–compression is used to calibrate the required quantities. Table 7 shows the calibrated material parameters for case 6, which was performed isothermally at 298 K. Figure 11 depicts the predicted stress–strain response that correlates fairly well and is fitted to the experiment.

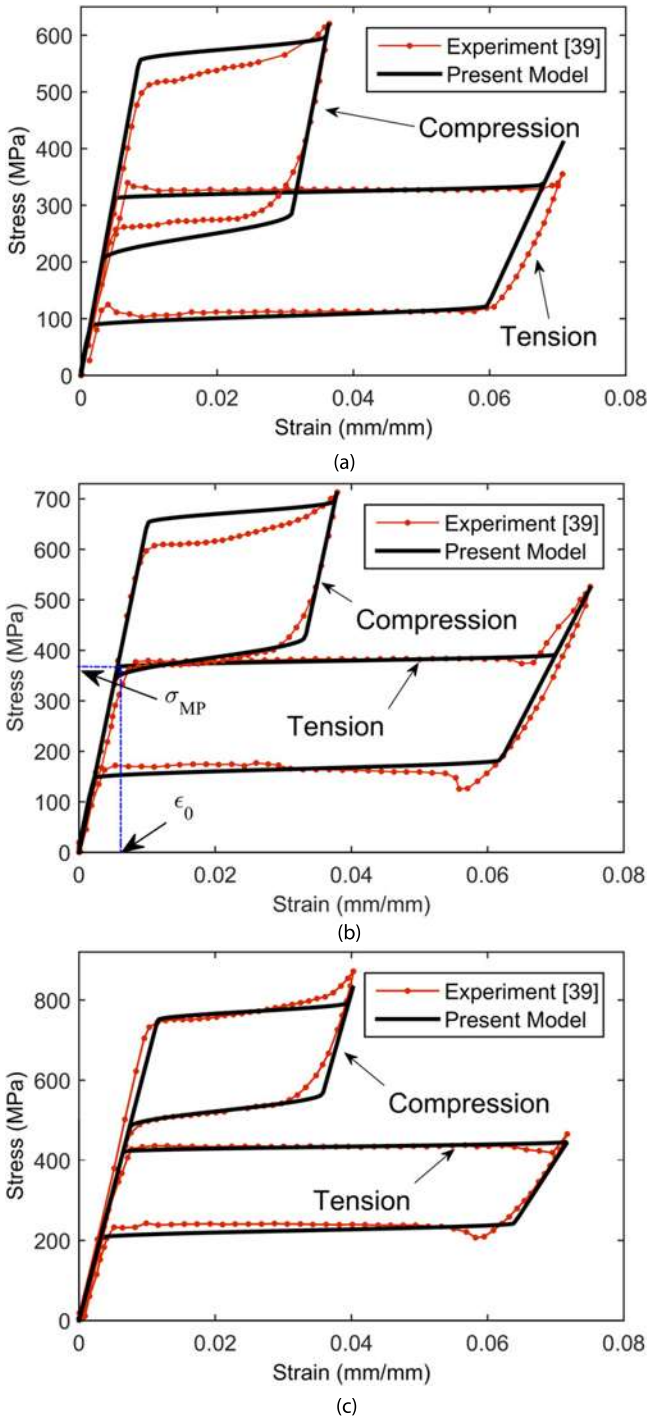

Figure 13. Comparison of numerical and experimental uniaxial tension–compression stress–strain responses at (a) T = 286 K (b) T = 296 K and (c) T = 306 K.

Table 8. Material parameters obtained by calibration of the stress–strain response in tension and compression for case 7.

E_A (MPa)	E_M^+ (MPa)	E_M^- (MPa)	ν	M_f (K)	M_s (K)	A_s (K)	A_f (K)	σ_s^{cr} (MPa)
65 000	26 000	62 000	0.3	213	253	265.6	271.6	130.2
σ_f^{cr} (MPa)	C_M (MPa/K)	C_{As} (MPa/K)	C_{Af} (MPa/K)	ε_L^+	ε_L^-	β_1	β_2	T (K)
155	5.5	6	6	0.057	−0.027	0.28	0.4	286, 296, 306

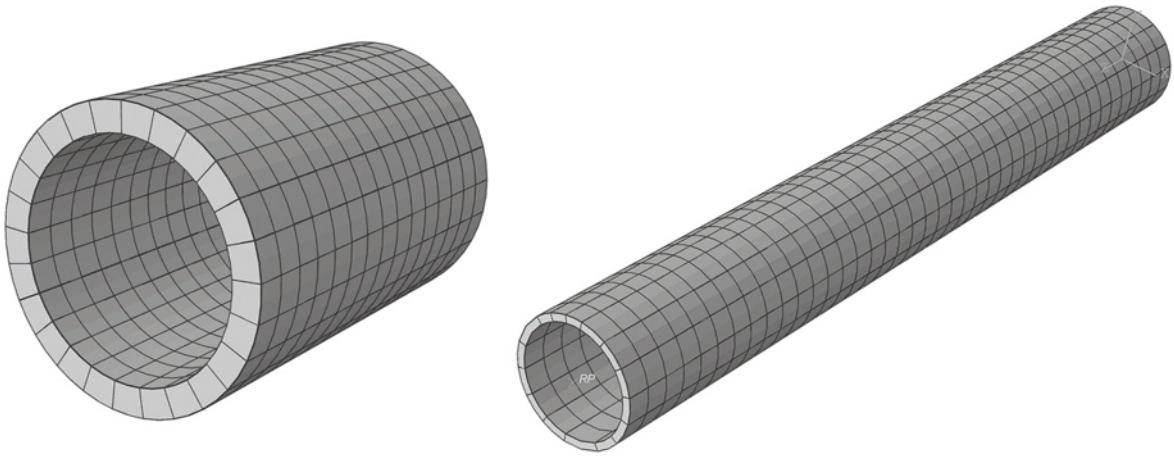

Figure 14. Final meshed model for (a) case 6 containing 375 elements and (b) case 7 containing 615 elements.

Since the experiments of case 7 are performed at several different temperatures, it is reasonable to develop the phase diagram for the tube used by Bechle and Kyriakides [39]. The reported uniaxial stress–strain responses at 286, 296, and 306 K are considered, and the phase diagram illustrated in figure 12 is obtained. According to the phase diagram as well as the stress–strain response at 306 K, the material parameters reported in table 8 are determined and are utilized to study case 7. Figures 13(a)–(c) show the uniaxial stress–strain responses using the material parameters presented in table 8. The comparison of the presented numerical predictions with the corresponding experimental findings demonstrates a good correlation between the results. It is worth mentioning that the phase diagram reported in figure 12 is obtained using the stress–strain response in tension. Therefore, the predictions of the model are closer to the experimental stress–strain curve during tension in comparison with compression.

The rest of the paper is allotted to the modeling of four-point bending in the above-mentioned cases. The models are meshed using 20-node quadratic brick reduced integration elements denoted by C3-D20R in ABAQUS. To reduce the effects of the mesh, the number of elements was refined until a negligible change was observed in the output results. Figures 14(a) and (b) show the final meshed model for cases 6 and 7 containing 375 and 615 elements, respectively.

Figure 15(a) shows variations of the normalized moment, MC/I, with the dimensionless curvature, $C\kappa$, where M is the reaction moment about the x-axis, I the corresponding area moment of inertia of the cross section, $C = D/2$ the outer radius of the tube, and $C\kappa = 2C\left(UR_1\right)/L_e$ the dimensionless curvature. Figure 15(b) compares the position of the neutral axis of the tube obtained using the proposed model with the experimentally measured one [40]. In this figure, the position of the neutral axis (Y_0) is measured from the centerline of the tube. In figures 15(a) and (b), a good agreement is observed for both moment and neutral axis position. The conformity is very good for small values of curvature. However, the conformity is good for higher values of curvature as well as in the unloading cycle; the predictions of the model are over-estimated in these regions. This may be due to the effects of strain localization in experimental measurements as reported in [40]. Since the present model is not capable of capturing this phenomenon, it over-predicts the amount of stress in high values of curvature. In addition, the length of the tube is not long enough in comparison with its diameter, and this causes the cross sectional planes not to remain planar. However, in the utilized model, all the degrees of freedom for the loading plane are tied to a reference point meaning that the plane remains planar. Therefore, the model is over-constrained in comparison with the real sample, and the required moment is over-predicted. As another reason, the transformation induced plasticity may cause some errors in finding the appropriate material parameters, especially maximum recoverable strain. Qidwai and Lagoudas [18] stated that plastic deformations occur before full Martensitic transformation takes place. Therefore, it is not possible to obtain the maximum recoverable strain using the experimental data. This issue can be one of the reasons for the difference between experimental

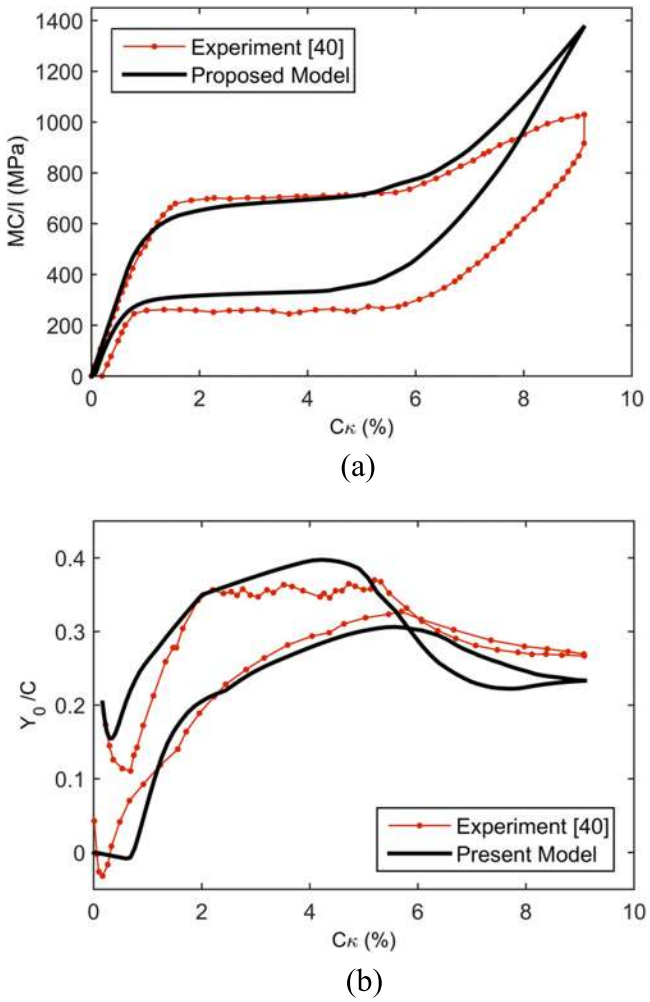

Figure 15. (a) Normalized moment versus dimensionless curvature and (b) normalized position of the natural axis versus dimensionless curvature for case 6.

and numerical observations in the unloading cycle. Auricchio and Taylor [17] reported that, for the case of four-point bending, the part of the curve corresponding to the unloading and the size of the hysteresis loop differ from the experimental findings.

To compare the numerical predictions with the experimentally reported results, the moment and curvature are normalized with the same method as the one used in experiments [39]. Referring to figure 13(b), suppose that σ_{PM} is the stress of the upper plateau, and ε_0 is the amount of strain at the beginning of the martensite transformation in tension at 296 K. Using these values, two quantities are defined for normalizing the moment and curvature, respectively, as $M_{o23} = \sigma_{PM} D_0^2 t$ and $\kappa_{o23} = 2\varepsilon_0/D$. In the first quantity, $D_0 = D - 2t$ is the inner diameter of the tube. Variations of the dimensionless moment with the dimensionless curvature for case 7 are depicted in figures 16(a)–(c) at 286 K, 296 K, and 306 K. The demonstrated results in this figure show the ability of the proposed model to predict the tension–compression asymmetry of shape memory alloys with good correlations with the experiment.

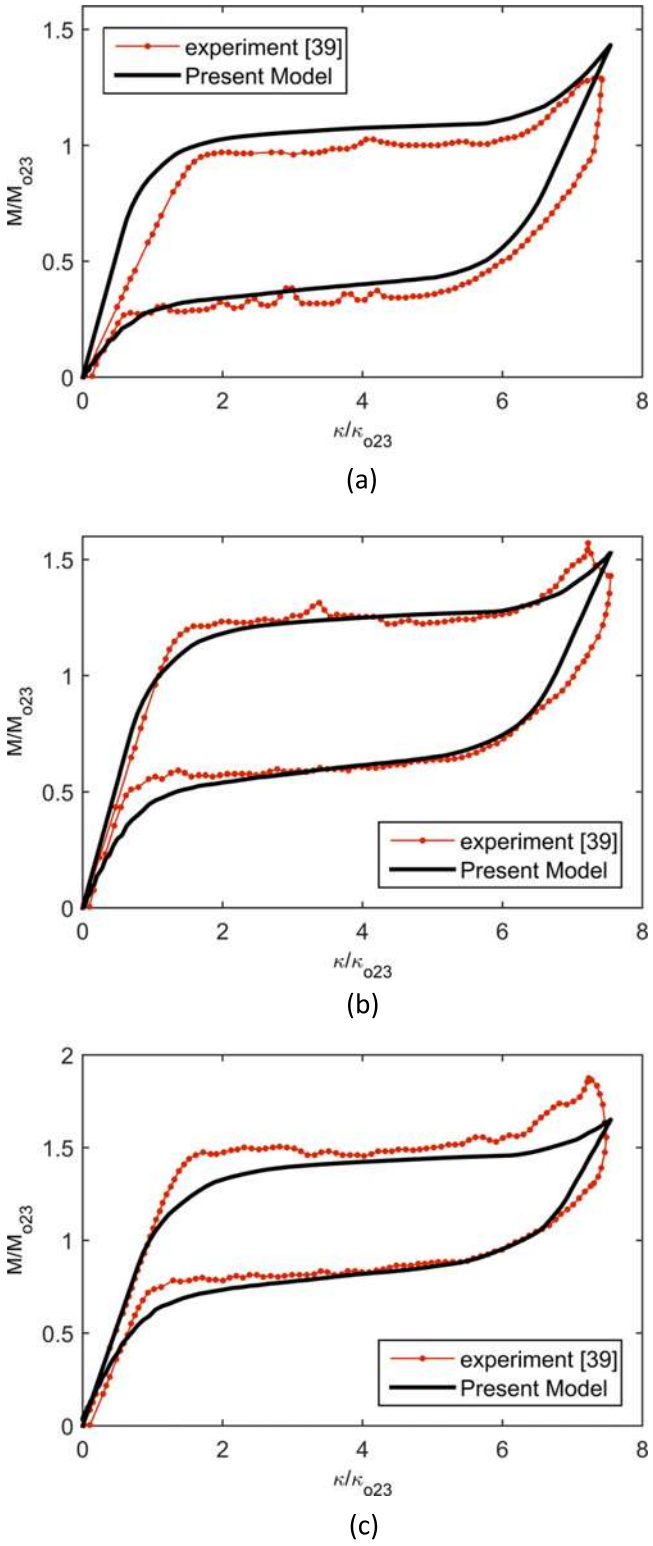

Figure 16. Variations of the dimensionless moment with the dimensionless curvature for case 7 in the temperatures of (a) 286 K, (b) 296 K and (c) 306 K.

Referring to figures 16(a)–(c), deviation of predicted response from the experiment increases, especially in the first linear region, as the temperature decreases. In all these simulations, the material is initially in the austenite phase and this deviation would be due to variations of austenite elastic

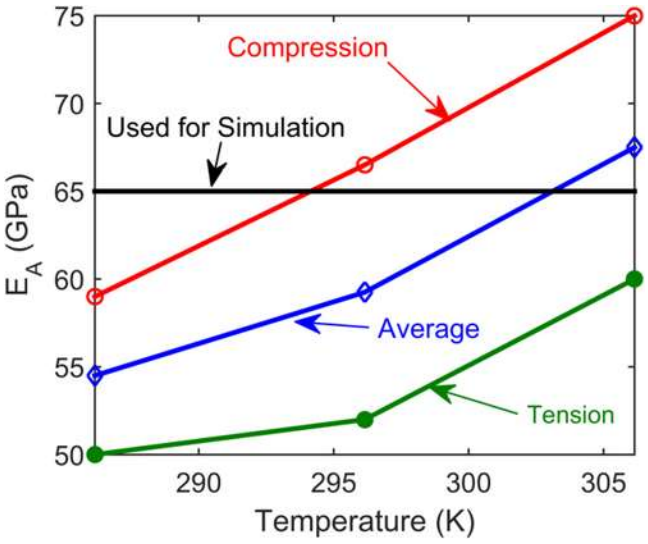

Figure 17. Variations of austenite elastic modulus with temperature.

modulus. Figure 17 shows the variations of austenite elastic modulus with temperature according to the experimental stress–strain curves provided in figure 13. As is obvious, E_A differs between tension and compression, which may have arisen due to the existence of some micro- (nano-) pores as well as defects in the microstructure of test samples [41, 42]. In addition, the experimental value of austenite elastic modulus increases with temperature. According to these findings, the difference between the numerical and experimental results in figure 16 can be explained. However, it should be stated that the present model cannot take different elastic moduli of austenite in tension and compression into account. Accordingly, only one fixed value is used through all the simulations. As shown in figure 17, the average value of E_A of tension and compression is smaller than the value used for the simulation at the temperatures of 286 and 296 K. Therefore, the numerically predicted value of the dimensionless moment is higher than the experimental one. However, for the temperature of 306 K, the average value of E_A is higher but not too far from that used for the simulation, which causes a better correlation with experimental observations. These findings demonstrate that, in order to obtain reasonable results, it is necessary to calibrate the elastic modulus of austenite based on the average value in tension and compression.

A comparison of the moment–curvature response for cases 6 and 7 reveals that the difference between the experiment and the presented model is larger for case 6. It might be owing to less accurate material parameters for case 6. Since there is just a uniaxial stress–strain curve at one temperature in case 6, it is not possible to find exact values of the required material parameters. However, in case 7, the existing stress–strain responses at three different temperatures makes it possible to develop a phase diagram and to find more accurate material parameters, which lead to a better correlation with experimental findings.

4. Conclusion

To account for material asymmetry in tension and compression, this paper proposes a new three-dimensional constitutive law based on microplane theory for shape memory alloys. The tension–compression asymmetry is taken into account by considering an equivalent stress based on $J_2 - J_3$ invarients. Also, two internal variables are defined to distinguish between martensite volume fraction as well as elastic modulus in tension and compression. The proposed model is then used for modeling the uniaxial tension–compression, ferroelastic problem, subloops due to incomplete transformation and four-point bending of SMA tubes. The obtained results are compared with experimental and previously-reported numerical ones. In each case, the results and their discrepancy are discussed. The findings of this study show that the model predictions are in good agreement with the experimental data, as well as the previously reported results by the existing models. In the case of four-point bending, some differences are observed between numerical and experimental findings, which could be due strain localization, distortion of the tubes cross section, transformation induced plasticity, variations of austenite elastic modulus with temperature, and different values of austenite elastic modulus in tension and comperession.

Acknowledgments

All the simulations were run at the National High-Performance Computing Center of Isfahan University of Technology. The authors would also like to thank Dr Ashrafizadeh for making it possible to use the facilities of this center.

References

[1] Bassani P, Panseri S, Ruffini A, Montesi M, Ghetti M, Zanotti C, Tampieri A and Tuissi A 2014 Porous NiTi shape memory alloys produced by SHS: microstructure and biocompatibility in comparison with Ti_2Ni and $TiNi_3$ *J. Mater. Sci. Mater. Med.* **25** 2277–85

[2] Köhl M, Bram M, Moser A, Buchkremer H P, Beck T and Stöver D 2011 Characterization of porous, net-shaped NiTi alloy regarding its damping and energy-absorbing capacity *Mater. Sci. Eng.* A **528** 2454–62

[3] Brown J 2014 SMA actuators: a viable practical technology *SMST: Proc. Int. Conf. on Shape Memory and Superelastic Technologies*

[4] Gilpin K, Torres-Jara E and Rus D 2014 Controlling closed-chain robots with compliant SMA actuators: algorithms and experiments *Experimental Robotics* (Berlin: Springer) pp 149–63

[5] Boyd J G and Lagoudas D C 1996 A thermodynamical constitutive model for shape memory materials: I. The monolithic shape memory alloy *Int. J. Plast.* **12** 805–42

[6] Brinson L 1993 One-dimensional constitutive behavior of shape memory alloys: thermomechanical derivation with non-constant material functions and redefined martensite internal variable *J. Intell. Mater. Syst. Struct.* **4** 229–42

[7] Liang C and Rogers C 1990 One-dimensional thermomechanical constitutive relations for shape memory materials *J. Intell. Mater. Syst. Struct.* **1** 207–34
[8] Tanaka K, Nishimura F and Tobushi H 1994 Phenomenological analysis on subloops in shape memory alloys due to incomplete transformations *J. Intell. Mater. Syst. Struct.* **5** 487–93
[9] Liang C and Rogers C 1992 A multi-dimensional constitutive model for shape memory alloys *J. Eng. Math.* **26** 429–43
[10] Graesser E and Cozzarelli F 1994 A proposed three-dimensional constitutive model for shape memory alloys *J. Intell. Mater. Syst. Struct.* **5** 78–89
[11] Lagoudas D C and Entchev P B 2004 Modeling of transformation-induced plasticity and its effect on the behavior of porous shape memory alloys: I. Constitutive model for fully dense SMAs *Mech. Mater.* **36** 865–92
[12] Panico M and Brinson L 2007 A three-dimensional phenomenological model for martensite reorientation in shape memory alloys *J. Mech. Phys. Solids* **55** 2491–511
[13] Popov P and Lagoudas D C 2007 A 3D constitutive model for shape memory alloys incorporating pseudoelasticity and detwinning of self-accommodated martensite *Int. J. Plast.* **23** 1679–720
[14] Arghavani J, Auricchio F, Naghdabadi R, Reali A and Sohrabpour S 2010 A 3D phenomenological constitutive model for shape memory alloys under multiaxial loadings *Int. J. Plast.* **26** 976–91
[15] Zhu Y and Dui G 2010 A macro-constitutive model of polycrystalline NiTi SMAs including tensile–compressive asymmetry and torsion pseudoelastic behaviors *Int. J. Eng. Sci.* **48** 2099–106
[16] Gall K, Sehitoglu H, Chumlyakov Y I and Kireeva I 1999 Tension–compression asymmetry of the stress–strain response in aged single crystal and polycrystalline NiTi *Acta Mater.* **47** 1203–17
[17] Auricchio F and Taylor R L 1997 Shape-memory alloys: modelling and numerical simulations of the finite-strain superelastic behavior *Comput. Methods Appl. Mech. Eng.* **143** 175–94
[18] Qidwai M and Lagoudas D 2000 On thermomechanics and transformation surfaces of polycrystalline NiTi shape memory alloy material *Int. J. Plast.* **16** 1309–43
[19] Auricchio F and Petrini L 2004 A three-dimensional model describing stress-temperature induced solid phase transformations: solution algorithm and boundary value problems *Int. J. Numer. Methods Eng.* **61** 807–36
[20] Bouvet C, Calloch S and Lexcellent C 2004 A phenomenological model for pseudoelasticity of shape memory alloys under multiaxial proportional and nonproportional loadings *Eur. J. Mech: A/Solids.* **23** 37–61
[21] Paiva A, Savi M A and Braga A M B 2005 Pacheco PMCL. A constitutive model for shape memory alloys considering tensile–compressive asymmetry and plasticity *Int. J. Solids Struct.* **42** 3439–57
[22] Lagoudas D C, Entchev P B, Popov P, Patoor E, Brinson L C and Gao X 2006 Shape memory alloys: II. Modeling of polycrystals *Mech. Mater.* **38** 430–62
[23] Lexcellent C, Boubakar M L, Bouvet C and Calloch S 2006 About modelling the shape memory alloy behaviour based on the phase transformation surface identification under proportional loading and anisothermal conditions *Int. J. Solids Struct.* **43** 613–26
[24] Saint-Sulpice L, Chirani S A and Calloch S 2009 A 3D super-elastic model for shape memory alloys taking into account progressive strain under cyclic loadings *Mech. Mater.* **41** 12–26
[25] Yu C, Kang G, Kan Q and Song D 2013 A micromechanical constitutive model based on crystal plasticity for thermo-mechanical cyclic deformation of NiTi shape memory alloys *Int. J. Plast.* **44** 161–91
[26] Mehrabi R, Kadkhodaei M and Elahinia M 2014 Constitutive modeling of tension-torsion coupling and tension–compression asymmetry in NiTi shape memory alloys *Smart Mater. Struct.* **23** 75021–35
[27] Brocca M, Brinson L and Bažant Z 2002 Three-dimensional constitutive model for shape memory alloys based on microplane model *J. Mech. Phys. Solids* **50** 1051–77
[28] Kadkhodaei M, Salimi M, Rajapakse R and Mahzoon M 2007 Microplane modelling of shape memory alloys *Phys. Scr.* **2007** 329
[29] Kadkhodaei M, Salimi M, Rajapakse R and Mahzoon M 2008 Modeling of shape memory alloys based on microplane theory *J. Intell. Mater. Syst. Struct.* **19** 541–50
[30] Mehrabi R and Kadkhodaei M 2013 3D phenomenological constitutive modeling of shape memory alloys based on microplane theory *Smart Mater. Struct.* **22** 025017
[31] Mehrabi R, Kadkhodaei M and Elahinia M 2014 A thermodynamically-consistent microplane model for shape memory alloys *Int. J. Solids Struct.* **51** 2666–75
[32] Mehrabi R, Kadkhodaei M, Andani M T and Elahinia M 2014 Microplane modeling of shape memory alloy tubes under tension, torsion, and proportional tension–torsion loading *J. Intell. Mater. Syst. Struct.* doi:10.1177/1045389X14522532
[33] Poorasadion S, Arghavani J, Naghdabadi R and Sohrabpour S 2013 An improvement on the Brinson model for shape memory alloys with application to two-dimensional beam element *J. Intell. Mater. Syst. Struct.* doi:10.1177/1045389X13512187
[34] Sameallah S, Kadkhodaei M, Legrand V, Saint-Sulpice L and Chirani S A 2014 Direct numerical determination of stabilized dissipated energy of shape memory alloys under cyclic tensile loadings *J. Intell. Mater. Syst. Struct.* doi:10.1177/1045389X14549869
[35] Thamburaja P and Anand L 2001 Polycrystalline shape-memory materials: effect of crystallographic texture *J. Mech. Phys. Solids* **49** 709–37
[36] Jaber M B, Mehrez S and Ghazouani O 2014 A 1D constitutive model for shape memory alloy using strain and temperature as control variables and including martensite reorientation and asymmetric behaviors *Smart Mater. Struct.* **23** 095026
[37] Nakanishi N, Mori T, Miura S, Murakami Y and Kachi S 1973 Pseudoelasticity in Au-Cd thermoelastic martensite *Phil. Mag.* **28** 277–92
[38] Takeda K, Tobushi H, Miyamoto K and Pieczyska E A 2012 Superelastic deformation of TiNi shape memory alloy subjected to various subloop loadings *Mater. Trans.* **53** 217–23
[39] Bechle N J and Kyriakides S 2014 Localization in NiTi tubes under bending *Int. J. Solids Struct.* **51** 967–80
[40] Reedlunn B, Churchill C B, Nelson E E, Shaw J A and Daly S 2014 Tension, compression, and bending of superelastic shape memory alloy tubes *J. Mech. Phys. Solids* **63** 506–37
[41] Karamooz Ravari M R and Kadkhodaei M 2015 A computationally efficient modeling approach for predicting mechanical behavior of cellular lattice structures *J. Mater. Eng. Perform.* **24** 245–52
[42] Karamooz Ravari M R, Kadkhodaei M, Badrossamay M and Rezaei R 2014 Numerical investigation on mechanical properties of cellular lattice structures fabricated by fused deposition modeling *Int. J. Mech. Sci.* **88** 154–61